Article

Polymer-Doped SnO₂ as an Electron Transport Layer for Highly Efficient and Stable Perovskite Solar Cells

Vo Pham Hoang Huy and Chung-Wung Bark *

Department of Electrical Engineering, Gachon University, Seongnam 13120, Gyeonggi, Republic of Korea;
vophamhoanghuy@yahoo.com.vn
* Correspondence: bark@gachon.ac.kr

Abstract: To produce highly efficient and repeatable perovskite solar cells (PSCs), comprehending interfacial loss and developing approaches to ameliorate interfacial features is essential. Nonradiative recombination at the SnO_2–perovskite interface in SnO_2-based perovskite solar cells (PSCs) leads to significant potential loss and variability in device performance. To improve the quality of the SnO_2 electron transport layer, a novel polymer-doped SnO_2 matrix, specifically using polyacrylic acid, was developed. This matrix is formed by spin-coating a SnO_2 colloidal solution that includes polymers. The polymer aids in dispersing nanoparticles within the substrate and is evenly distributed in the SnO_2 solution. As a result of the polymer addition, the density and wetting properties of the SnO_2 layer substantially improved. Subsequently, perovskite-based photovoltaic devices comprising SnO_2 and Spiro-OMeTAD layers and using $(FAPbI_3)_{0.97}(MAPbBr_3)_{0.03}$ perovskite are constructed. These optimized devices exhibited an increased efficiency of 17.2% when compared to the 15.7% power conversion efficiency of the control device. The incorporation of polymers in the electron transport layer potentially enables even better performance in planar perovskite solar cells.

Keywords: perovskite solar cells; tin oxide; electron transport layers; polyacrylic acid; doping materials

1. Introduction

Metal halide perovskite has emerged as a key technology for high-performance optoelectronic devices, owing to its long diffusion length and high defect tolerance [1–4]. Recent advancements have seen perovskite solar cells (PSCs) achieve a rapid increase in power conversion efficiency (PCE), reaching up to 26% [5–7]. This progress parallels the optimal standard of commercial silicon cells [8]. Planar PSCs are becoming increasingly prominent and competitive in the photovoltaic field due to their simple synthesis process, low cost, and high efficiency [9–12]. However, challenges such as significant photocurrent hysteresis and unstable output under operational conditions remain major concerns for many planar PSCs [13–15]. These issues are largely attributed to ion migration and suboptimal interfacial properties in the devices [16,17]. Many studies have underscored the importance of smooth and dense surfaces for efficient electron transport and effective hole blocking, which prevents holes from moving from the absorber layers to the transparent electrode [18,19]. Consequently, there is a strong consensus on the necessity of designing optimal electron transport.

The ETL plays a vital role in PSC performance. To inhibit carrier recombination, the ETL must simultaneously prevent the migration of carriers to the counter electrode and facilitate the charge transport process from the photoactive layer to the electrode. Specifically, TiO_2, ZnO, Nb_2O_5, Zn_2SO_4, Fe_2O_3, In_2O_3, and SnO_2 are widely used ETLs in PSCs. The specific performance of varied types of ETL is presented in detail in Table 1.

Table 1. Device structure and performance parameters of different metal oxide ETLs.

ETL	Structure of Device	PCE (%)	V_{OC} (V)	J_{SC} (mA cm^{-2})	FF	Ref
TiO_2	$FTO/TiO_2/MAPbI_3/Spiro-OMeTAD/Au$	20.9	1.17	23.31	0.77	[20]
ZnO	$ITO/ZnO/PBDB-T:ITIC/MoO_3/Ag$	16.9	0.88	14.6	0.63	[21]
Nb_2O_5	$ITO/NiO_x/FA_{0.85}MA_{0.15}PbI_{2.55}Br_{0.45}/Nb_2O_5/Ag$	18.3	1.08	22.7	0.72	[22]
Zn_2SO_4	$ITO/Zn_2SnO_4/PCBM/CH_3NH_3PbI_3/Spiro-OMeTAD/Ag$	14.5	1.07	21.2	0.62	[23]
Fe_2O_3	$FTO/Fe_2O_3/CH_3NH_3PbI_3/Spiro OMeTAD/Au$	10.78	0.65	16.6	0.63	[24]
In_2O_3	$FTO/In_2O_3/CH_3NH_3PbI_3/Spiro-OMeTAD/Au$	13.97	1.07	19.3	0.68	[25]
SnO_2	$FTO/SnO_2/(FAPbI_3)_{0.95}(MAPbBr_3)_{0.05}/Spiro-OMeTAD/Au$	20.6	1.08	24.42	0.78	[26]

Despite an increase in the number of semiconductor materials that are being discovered and applied for ETL in PSC, TiO_2 and SnO_2 have been extensively used as ETLs due to their superior properties. Mesoporous TiO_2 coated over compact TiO_2 was initially used as the electron transport material for PSCs, originating from solid-state dye-sensitized solar cells [27]. Nevertheless, the low electron mobility of TiO_2 as well as high-temperature annealing have both negative and detrimental effects on the future application of PSCs [28–31]. Additionally, the strong effects of photocatalytic TiO_2 require special attention because they reduce the stability of PSC under illumination [32,33]. Recently, SnO_2 has been widely used as the most promising ETL, with a proven efficiency of over 21% and a substantial reduction in photocatalytic and hysteresis issues under illumination [34,35]. SnO_2 exhibits the typical properties of an ideal ETL with high mobility [up to 240 cm^2/(V·s)], large bandgap (exceeding 3.6 eV), and excellent chemical stability, making it a strong candidate for highly efficient PSCs [36,37]. However, SnO_2 is inherently an insulating material when processed at low temperatures, and the efficiency of the device is heavily dependent on the thickness of the SnO_2 layer [38–41]. To achieve fast charge transfer, high-performance SnO_2-based PSCs require a thin SnO_2 layer that is less than 30 nm in thickness. The aggregation issue of the nanoparticles in the film makes it difficult to fabricate such a thin and compact layer using the spin-coating technique [42–44]. Typically, the resulting SnO_2 thin film has extensive areas of nonuniformity and pinholes. Additionally, pretreatment (such as UV treatment) is necessary to change the poor wetting performance of SnO_2 with the perovskite precursor solution.

Doping organic compounds into electron transport layers (ETLs) can either align the Fermi level of the ETL with the conduction band of perovskite or influence the perovskite/hole transport layers, improving the crystallization and grain size of the perovskite layer [45–47]. Thus, doping effectively lowers trap defects in the photo absorber and ETL, enhancing charge separation and transfer for efficient perovskite solar cell performance. Based on this approach, polyethylenimine ethoxylate (PEIE) was utilized to enhance the electron transport capacity of SnO_2 by suppressing trap-assisted recombination and lowering the energy barrier between the active layer, as well as improving the wetting ability of these layers, resulting in high PSC performance [48]. Additionally, incorporating polyethylene glycol (PEG) promoted the separation of nanoparticles in the film and significantly improved the density and wetting properties of the SnO_2 layer, leading to an improvement in device performance [49]. Furthermore, polyvinyl pyrrolidone (PVP), another water-soluble polymer, was also used for this purpose [50]. The formation of bonds between the electron pairs of nitrogen (or oxygen) in PVP and metal ions enables PVP to adhere to metal surfaces, while the long vinyl polymer chain of the PVP backbone prevents nanoparticle agglomeration through steric hindrance [50].

Given these challenges, doping the ETL with polymers to create a uniform and compact SnO_2 ETL and enhance the PCE of devices is valuable. PAA polymer has been extensively used in various energy storage technologies, such as electrolytes in flexible symmetrical supercapacitors, novel separators in silver oxide batteries, or as binders for GaP anodes in lithium-ion batteries [51–53]. However, the use of PAA as a doping material in SnO_2 colloidal precursors for PSCs has not been explored. We propose that integrating PAA

with the SnO_2 colloidal solution could help in forming an effective ETL. Additionally, we present the development of an ideal PAA@SnO_2 ETL, combining SnO_2 with Li-ion. By selecting water-soluble polymers such as PAA, which dissolve in the SnO_2 colloidal aqueous solution, we discovered that the PAA chain effectively limits the aggregation of SnO_2 nanoparticles in the precursor solution. This combination with polymers substantially improves the quality of the film, enhancing its compaction and wetting properties.

2. Experiment Section

2.1. Materials

Lead Iodide (PbI_2), Lithium chloride (LiCl), spiro-oMeTAD (99.8%), methylammonium bromide (MABr), methylammonium chloride (MACl), chlorobenzene (CB), isopropanol (IPA), DMSO, DMF, acetonitrile (ACN), lithium bis(trifluoromethanesulfonyl) imide (Li-TFSI), and 4-tert-butyl were purchased from Sigma-Aldrich (Seoul, Republic of Korea). A SnO_2 colloidal solution (15 wt% in water) was purchased from Alfa Aesar (Seoul, Republic of Korea). Formamidinium iodide (FAI) was purchased from GreatCell Solar (Queanbeyan, Australia).

2.2. Perovskite Solar Cell Fabrication

The preparation of PSC is shown in detail in Figure 1. The glass/FTO substrate was cleaned using distilled water, acetone, and isopropanol. Then, the FTO glasses were dried using a nitrogen gun and treated with UV–ozone for 20 min. The SnO_2 precursor was obtained by dissolving SnO_2 (450 μL) colloid dispersion and LiCl (300 μL) aqueous solution (17 mg/4 mL) in water (2 mL) [49]. For PAA@SnO_2, PAA (0.5, 1.0, 2.0, and 3.0 mg/mL) was added into the SnO_2 precursor solution. The SnO_2-based electron transport layer was spin-coated on the cleaned FTO at 3000 rpm for 30 s. This was followed by annealing at 150 °C for 30 min in air. Then, the substrates were treated with UV–ozone for 20 min before being transferred into a glovebox. The perovskite films were fabricated using a typical two-step sequential deposition method. First, 50 μL of PbI_2 precursor solution (600 mg PbI_2 dissolved in (DMF 0.9 mL) and (DMSO 0.1 mL)) was spin-coated onto SnO_2 films at 2000 rpm for 20 s. The FAI/MABr/MACl mixed solution (60 mg FAI, 6 mg MABr, and 6 mg MACl dissolved in 1 mL IPA) was spin-coated onto the PbI_2 film at 4000 rpm for 20 s. Then, the films were annealed at 150 °C for 20 min. After cooling to room temperature, the hole-transport layer was subsequently deposited on top of the perovskite film via spin-coating at 4000 rpm for 40 s using a chlorobenzene solution, which contained Spiro-OMeTAD (72.3 mg mL^{-1}), tert-butylpyridine (29 μL mL^{-1}), and bis(trifluoromethane)sulfonimide lithium salt (18.5 μL mL^{-1}, 520 mg mL^{-1} in acetonitrile). Finally, 100 nm of gold electrodes were deposited on top of the devices via evaporation at approximately 10^{-6} Torr.

2.3. Characterization

To assess the ability of film to absorb light, the UV–Vis spectrophotometer Agilent (Varian, Cary 50, San Diego, CA, USA) was used to measure the UV–Vis light-absorption spectra of film. The X-ray diffraction (XRD) patterns were acquired using an XRD Rigaku DMAX 2200 system (Tokyo, Japan) with Cu K as the X-ray source (λ = 0.15406 nm). The Fourier transform infrared (FTIR) spectra were captured using an infrared spectrometric analyzer (Vertex 70, Bruker, Karlsruhe, Germany). Field emission scanning electron microscopy (FESEM, Hitachi S-4700, Tokyo, Japan), operating at 10 kV, was used to analyze the top and cross-sectional morphologies of the samples. Using a QuantaMaster TM 50 PTI (Piscataway, NJ, USA), steady-state photoluminescence (PL) spectra were acquired. A solar simulator (McScience K3000, Solar Simulator LAB 50, and Polaromix, Gyeonggi, Republic of Korea) simulating solar radiation with an irradiance of 100 mW cm^{-2} (AM 1.5 G) was used to model sunlight conditions. The external quantum efficiency (EQE) was determined using a McScience K3100 measurement system (Suwon, Republic of Korea).
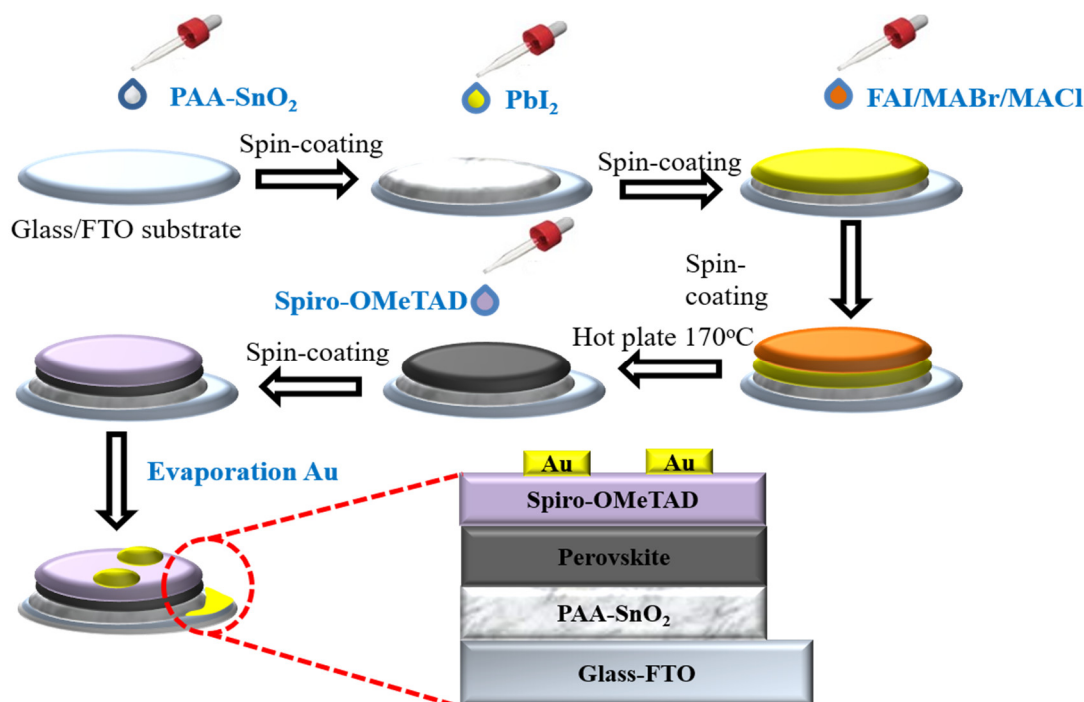
Figure 1. Schematic illustrating the process of preparing complete solar cell.

3. Results and Discussion

Despite semiconductor oxide nanoparticles being recognized as potential electron transport layer (ETL) materials for perovskite solar cells (PSCs), their tendency to agglomerate due to van der Waals forces within the colloid, coupled with their large specific surface area, presents a significant challenge [54,55]. Various strategies, including doping and surface engineering, have been implemented to curb the agglomeration of SnO_2 particles in dispersion systems with small-sized particle media, thereby stabilizing SnO_2 colloids. The suspension, uniformity, and stability of nanoparticles in water are heavily influenced by particle spatial agglomeration and charge balance. Introducing a suitable polymer or surfactant material helps to reduce inter-particle space and maintain a uniform charge on the particle surfaces, thus preventing oxide nanoparticle agglomeration. In this context, PAA is used as a buffering agent to stabilize SnO_2 particles, working through two mechanisms: (i) PAA reduces the available active space around the particles, preventing SnO_2 nanoparticle agglomeration, and (ii) crucially, functional groups on the PAA surface, when combined with SnO_2 nanoparticles, help balance the charge between particles. To explore the impact of PAA on the photovoltaic characteristics and enhance PSC performance, a range of material characterization techniques were applied, as detailed throughout this manuscript.

We initially investigated the surface morphology obtained on different ETLs (SnO_2 and PAA@SnO_2) (as shown in Figure 2). Compared with the FTO surface (Figure 2a), SnO_2 and PAA@SnO_2 were successfully prepared (Figure 2b,c). However, the PAA@SnO_2 nanocrystals were densely coated, and there were no pinholes on the film surface. This can prevent ineffective contact between the ETL film surface and perovskite, leading to improved optical performance. The EDX analysis presents the existing components on the PAA@SnO_2 film (Figure 2d). The presence of a small amount of residual Cl (2.25%) does not significantly affect the composition of the film due to the guaranteed elemental ratio between Sn and O (specifically SnO_2) along with the existence of PAA on the FTO substrate. Furthermore, Figure 2e shows the elemental mapping spectra corresponding to PAA@SnO_2 film, showing the uniform distribution of Sn, O, and C nanocrystals throughout the film.
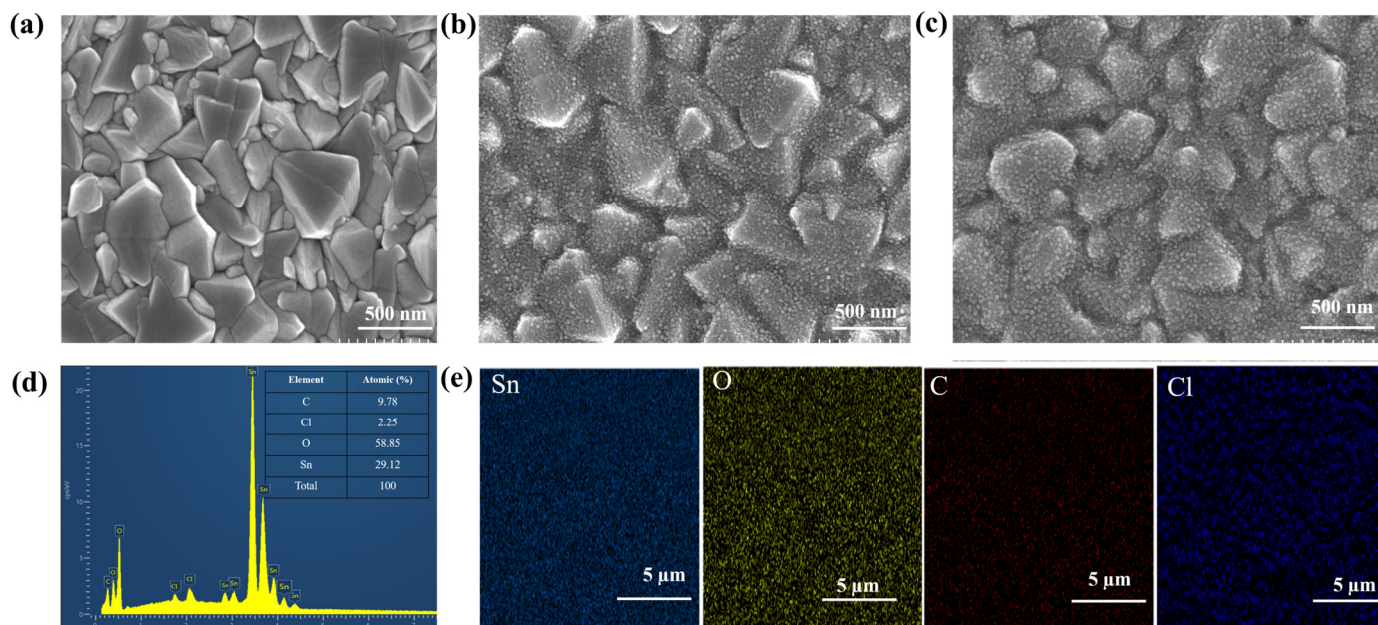
Figure 2. SEM image of (**a**) pristine FTO, (**b**) FTO/SnO$_2$, (**c**) FTO/PAA@SnO$_2$, (**d**) EDX spectrum of PAA@SnO$_2$, and (**e**) elemental mapping corresponding to PAA@SnO$_2$ on FTO/glass.

XRD analysis was performed to obtain crystallographic information regarding as-synthesised pure SnO$_2$ and PAA@SnO$_2$. Figure 3 displays the acquired XRD patterns for PAA@SnO$_2$ and pristine SnO$_2$. The main diffraction peaks at approximately 26.25°, 33.66°, 38.16°, 51.50°, 54.82°, and 61.55° for pure SnO$_2$ correspond to (110), (101), (200), (211), (310), and (301), respectively. This indicates that a pure rutile tetragonal SnO$_2$ structure has formed (JCPDS no. 41–1445). When a low concentration of PAA was added as a dopant, no additional peak was observed in the PAA@SnO$_2$, indicating that PAA doping did not introduce a secondary phase as an impurity with the pure SnO$_2$. Conversely, a reduction in peak intensity was observed in PAA@SnO$_2$ spectrum, likely resulting from the interaction between the PAA polymer and SnO$_2$ crystals.

Thermogravimetric analysis (TGA) and differential scanning calorimetry (DSC) were used to determine the thermal properties of FTO, FTO/SnO$_2$, and FTO/PAA@SnO$_2$ from 25 °C to 700 °C in nitrogen gas flowing at a rate of 10°/min. Figure 4a shows that the FTO substrate remains stable in N$_2$ up to 700 °C. This indicates good thermal stability without pyrolysis or thermo-oxidative decay occurring. However, conducting investigations at temperatures above 700 °C is not advisable, as this can lead to a decrease in Hall mobility and reduction in the number of oxygen vacancies. These changes result in lower mobility and fewer carriers in the FTO membrane, ultimately leading to the increased resistivity of the FTO substrate [56]. Additionally, the spin-coating of SnO$_2$ and PAA@SnO$_2$ forms thin films of 69 and 35 nm, respectively. Thus, the mass loss is not too significant, specifically 99.98% (Figure 4b) and 99.94% (Figure 4c). Furthermore, the obtained curve of the DSC analysis is very similar. In Figure 4a–c, the DSC plot shows two endothermic peaks. The first endothermic peak is approximately in the range of 45–110 °C, corresponding to the removal of the absorbed water from the substrate [57,58]. The other small peak at 580 °C was due to further crystallinity of the FTO substrate [59,60]. Therefore, the degree of SnO$_2$ and PAA@SnO$_2$ crystallization on the FTO substrate is appropriate for the annealing temperature of 150 °C.
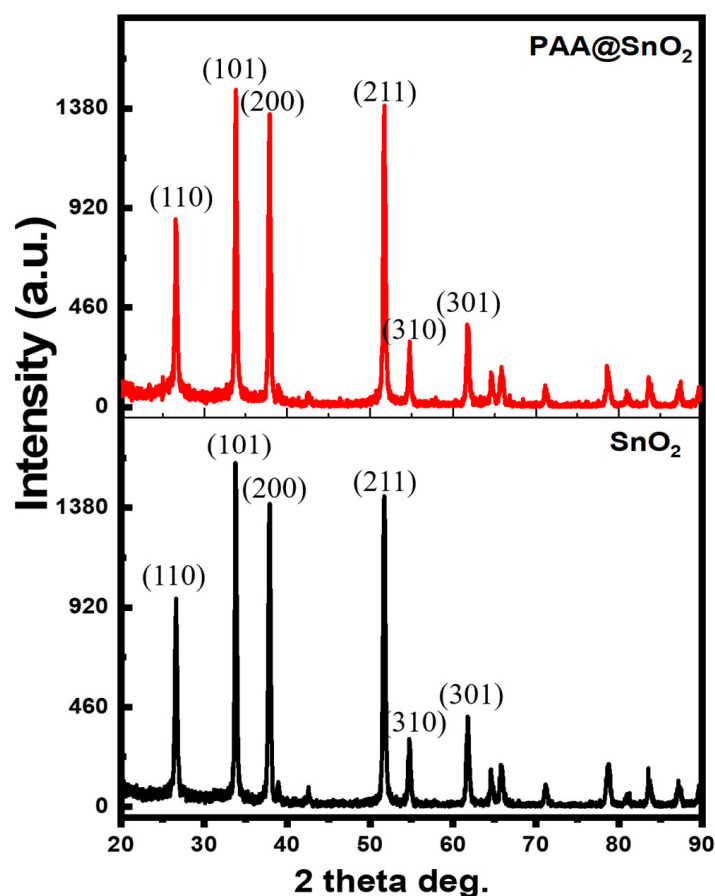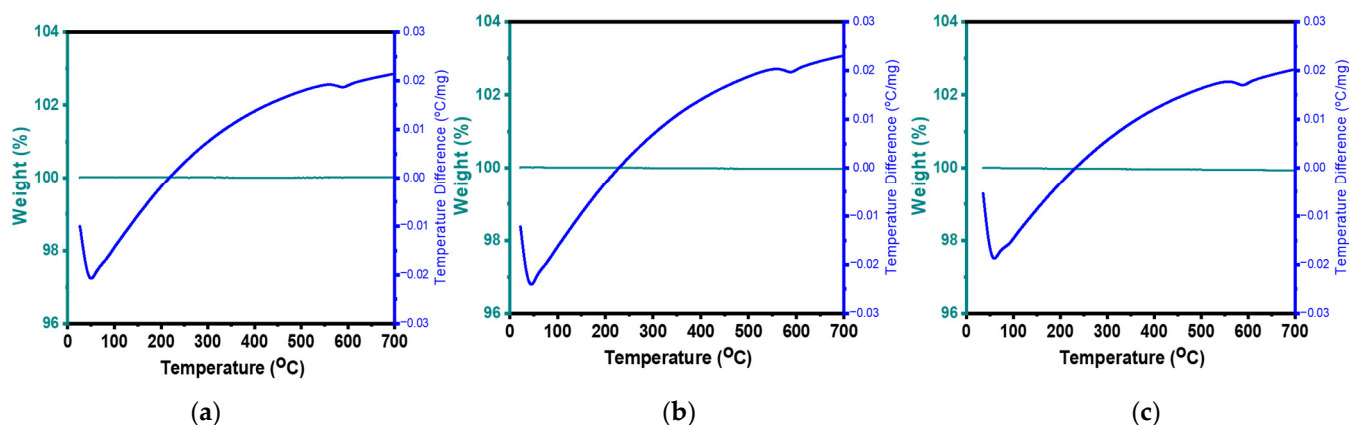
Figure 3. XRD pattern of SnO_2 and PAA@SnO_2.

Figure 4. Thermal properties of (**a**) FTO, (**b**) FTO/SnO_2, and (**c**) FTO/PAA@SnO_2.

Next, to investigate the influence as well as find the optimal concentration of PAA, we adjusted the PAA concentration to 0.5, 1.0, 2.0, and 3.0 mg mL^{-1}, respectively. The undoped or doped SnO_2 ETL were spin-coated with SnO_2 precursor solution at ambient temperature and then thermally annealed in air for 30 min at 170 °C. The chemical structure of PAA-SnO_2 is shown in Figure 5.
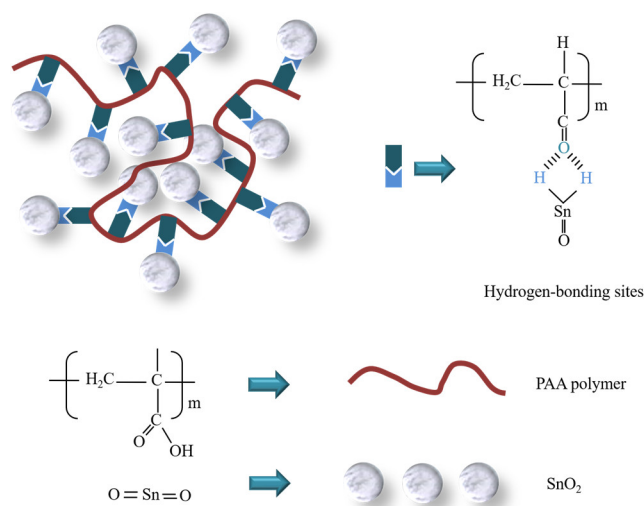
Figure 5. Chemical structure of SnO_2 and PAA@SnO_2.

Figure 6a shows a facile synthesis of ETL used to collect and transport electrons from the absorber layer to the TCO. First, the ability to transmit in the visible region of pristine SnO_2 and PAA@SnO_2 at different concentrations was evaluated. From Figure S1a, undoped and doped SnO_2 ETL show excellent transmittance in the wavelength region from 300–900 nm, and the transmittance of the PAA@SnO_2 at various film concentrations almost remains unchanged when compared with that of the pristine SnO_2 film. This indicates that the addition of PAA slightly changes the optical transmittance properties of the undoped SnO_2 film. Additionally, a good transmittance spectrum is advantageous to the performance of PSCs because it shows uniform film deposition with few defect states. However, a minor decrease in the transmittance of the ETL is observed, corresponding to the optical image of the solution shifting from transparent to opalescent with the increasing doping concentration of PAA, as illustrated in Figure S1b. Additionally, the absorbance progressively increases as the wavelength increases, as shown in Figure S2a. The Tauc plot (Figure S2b) was utilized to estimate the optical band edge (E_g). It was determined that the E_g of the pristine SnO_2 film was 4.2 eV. This value remained nearly unchanged for PAA@SnO_2, suggesting that the small amount of PAA doping did not significantly impact the E_g of the pristine SnO_2 film.

Fourier transform infrared (FT-IR) spectroscopy was analyzed to determine the presence of separate components in the PAA@SnO_2 film before annealing (Figure 6b). The O-Sn-O stretching mode and Sn-O vibrational mode are responsible for the absorption peaks at 550, 650, 1550, and 1690 cm^{-1}, respectively [49]. The COOH stretching modes in PAA are responsible for the peaks to appear at 1479, 1296, and 948 cm^{-1}. It can be seen that PAA was absorbed into SnO_2 film by noting that the spectrum of PAA@SnO_2 exhibits the typical peaks of SnO_2 and PAA, with the O-Sn-O peaks of SnO_2 shifting to 670 cm^{-1}. Furthermore, the presence of PAA at different concentrations in the SnO_2 precursor solution was demonstrated by the FT-IR spectrum (Figure S3). More importantly, we explored whether annealing plays a role in the formation of PAA@SnO_2. According to Figure S4, there is a slight change in the composition of pristine SnO_2 and PAA@SnO_2 at various concentrations post-annealing. Notably, the presence of hydroxyl groups on the film surface at 2850 and 2915 cm^{-1} indicates strong hydrogen bonding with the carboxylic group in the PAA polymer. This is attributed to the high temperature of the annealing process, which promotes the partial breakdown of the Sn=O bond, leading to the formation of Sn(OH)n on the SnO_2 surface. The mechanism of this hydrogen bond formation is depicted in Figure 6c. Therefore, during the annealing process, the hydroxyl group on the SnO_2 surface forms a hydrogen bond with the carboxylic group of PAA (as shown in Figure 5) [49,53,61].
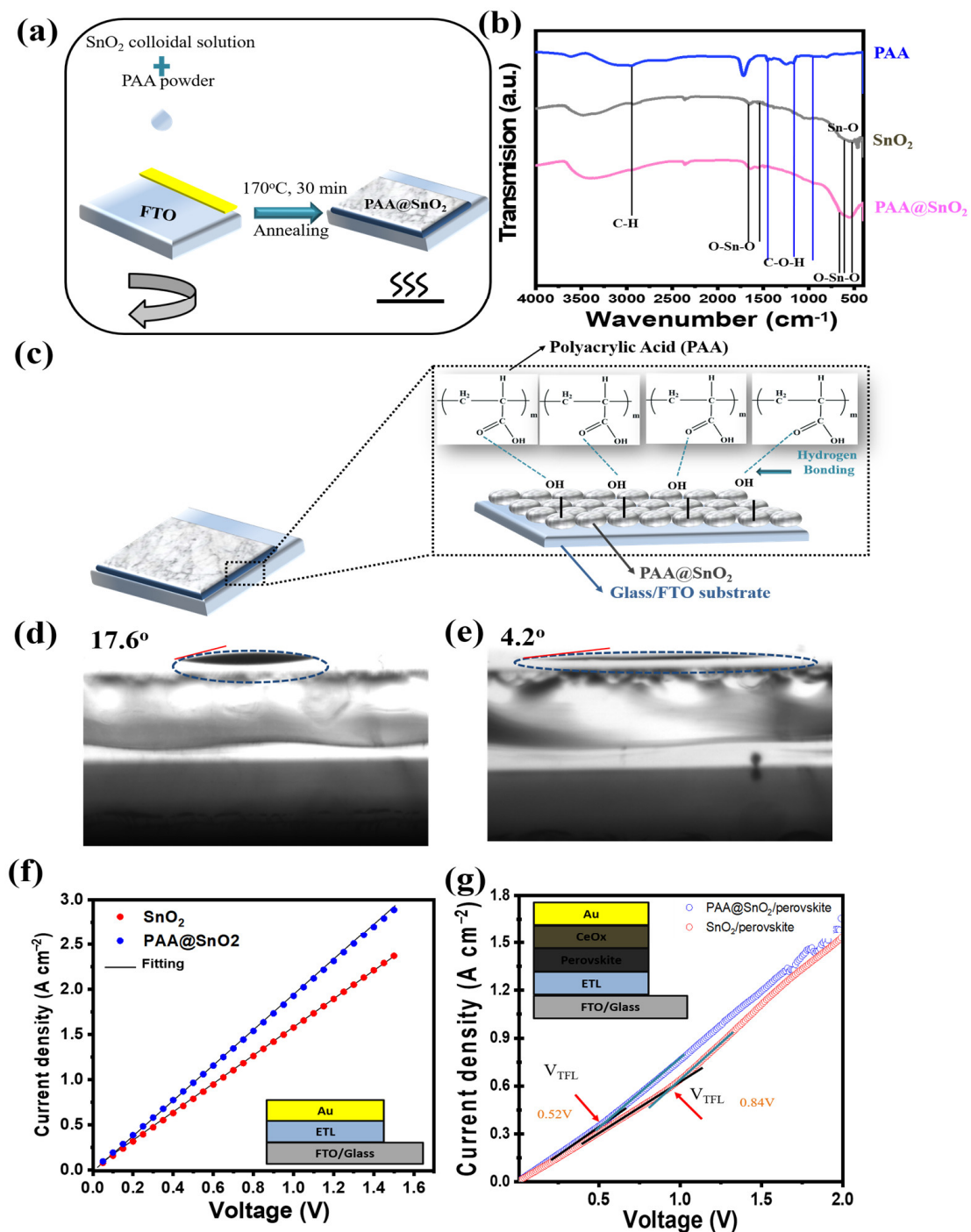
Figure 6. (**a**) Schematic illustrating the pristine and PAA@SnO$_2$ ETL preparation. (**b**) FT-IR spectra of PAA, SnO$_2$, and PAA@SnO$_2$ films before annealing. (**c**) Diagram of mechanism for hydrogen bond formation. Contact angle measurement of SnO$_2$ films without (**d**) or with (**e**) PAA polymer (blue circle: boundary region to determine the contact angle). (**f**) The electron mobility for the SnO$_2$ and PAA@SnO$_2$ films calculated by the SCLC model with the device structure of Glass/FTO/ETL/Au. (**g**) Dark I-V measurement of the electron-only devices based on SnO$_2$ and PAA@SnO$_2$ ETLs.

By suppressing the formation of large clusters in the substrate and using SnO$_2$ that has been incorporated into PAA via hydrogen bonding, it is anticipated that the spin-coated film will become compact and uniform with a decrease in pinholes and that the PAA polymer will create a dense and compact matrix on the substrate. Additionally, to obtain complete coverage on the substrate, UV pretreatment is required because pure SnO$_2$ film

is a non-wettable surface for a perovskite precursor solution. This implies that the water contact angle measurement of pristine SnO_2 is high (approximately 40°) [62,63] and clearly decreases after UV treatment (17.6°). Fortunately, PAA inclusion in SnO_2 film can enhance the affinity between SnO_2 and perovskite by altering the SnO_2 surface, as demonstrated in Figures 6d,e and S5. Therefore, increasing PAA concentration will contribute to further reducing contact angle of SnO_2. However, excessively increasing the PAA concentration (specifically 3 mg/mL) will promote particle aggregation, leading to a rebound increase in contact angle data. When compared to PAA@SnO_2 at various concentrations, the contact angle of the perovskite solution on pure SnO_2 film was significantly higher. Additionally, perovskite is not completely coated on the virgin SnO_2 substrate without pretreatment. However, perovskite on PAA@SnO_2 displays a dense and compact coating (Figure S6). Hence, without any pretreatment (such as UV treatment), a complete covering of perovskite film on the PAA@SnO_2 layer is accomplished.

The effect of PAA on the conductivity of the SnO_2 thin films was analyzed via electrical measurements. As shown in Figure 6f, the PAA@SnO_2 film exhibits a higher electron mobility (2.08×10^{-3} cm^2 V^{-1} s^{-1}) than that of the SnO_2 film (8.5×10^{-4} cm^2 V^{-1} s^{-1}) as measured by the space charge limited current (SCLC) method [36,64]. The SCLC model was used with the electron-only devices (FTO/ETL/perovskite/CeO_x/Au) to investigate the trap density [65]. The dark I-V curves for the two devices are displayed in Figure 6g. Typically, the I-V curve exhibits a linear ohmic-type response at low bias voltages. The current begins to increase nonlinearly with an increase in bias voltage, signaling the commencement of the trap-filling process. Furthermore, trap-filled limit voltage (V_{TFL}) is the definition of the kink point that separates the linear and nonlinear regions. The trap density (N_t) can be computed using the following equation:

$$N_t = \frac{2\, \varepsilon_0 \varepsilon\, V_{TFL}}{e\, L^2}$$

where ε_0, ε, e, and L denote the perovskite film thickness, elementary charge, relative dielectric constant, and permittivity of vacuum, respectively. The perovskite layer on the PAA@SnO_2 ETL has an estimated trap density of approximately 6.27×10^{14} cm^{-3}, which is significantly less than the 4.4×10^{15} cm^{-3} of the film deposited on the SnO_2 ETL, indicating that the introduction of PAA reduces the defect states of the ETL.

With or without PAA doping, compact SnO_2 films were spin-coated onto FTO substrates using a colloid dispersion solution. To better understand the surface morphology of the coated films, atomic force microscopy (AFM) was employed. Given that FTO shows a roughness surface of 30 nm [66,67], both SnO_2 ETL films exhibit a smooth surface, as observed in Figure S7a,b. However, a pristine SnO_2 film exhibits a rougher surface than the SnO_2 ETL films (26.32 nm vs. 24.98 nm), which is in line with the surface morphology observed via scanning electron microscopy (SEM), as shown in Figure 2b,c. Furthermore, it should be observed that at a concentration of 0.5 mg mL^{-1}, several pinholes are visible, despite the fact that the agglomeration between particles is significantly reduced when compared to pristine SnO_2 (as shown in Figure 7a). This result suggests that the SnO_2 oligomers can be disaggregated by the hydrogen bonds of PAA and SnO_2 particles. However, their affinity is insufficient to glue the particles together. When the concentration increases slightly (1.0 mg mL^{-1}), the PAA@SnO_2 surface is pinhole-free with no intergranular agglomeration through uniform particle formation (Figure 7b). Additionally, due to the high hydrogen bonding affinity between PAA and SnO_2, which occurred when the mass concentration of PAA exceeded 1.0 mg mL^{-1} or when there were more PAA components present, PAA@SnO_2 aggregated into large particles and failed to form a uniform and dense ETL layer in Figure 7c–d.
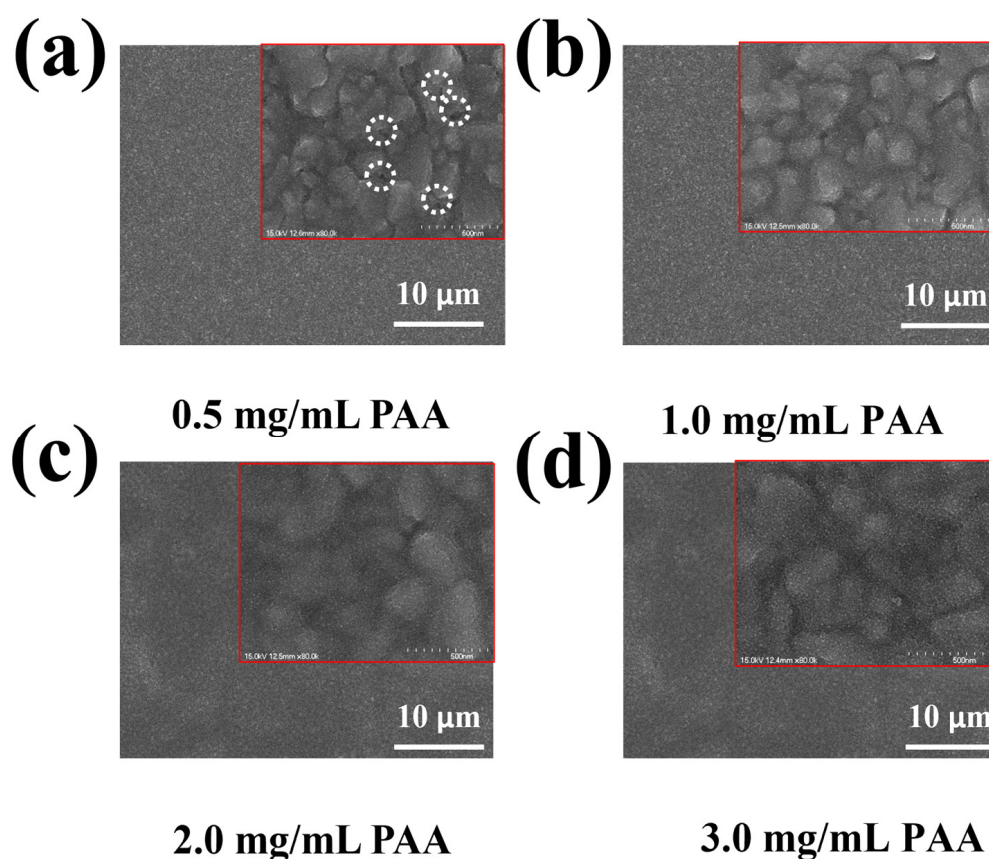
Figure 7. Top-view SEM image of (**a**) pristine SnO_2 (dashed circles: pinholes on the surface) and (**b–d**) PAA@SnO_2 at various concentrations (red squares: high-magnification SEM image).

AFM measurements revealed that the root mean square (RMS) roughnesses of perovskite films on SnO_2 and PAA@SnO_2 were 25.19 nm and 24.73 nm, respectively. This smoother perovskite is shown in Figure 8a,b. The SEM images of the absorber layer deposited onto various ETLs are shown in Figure 8c,d. The images confirm the surface morphology of the perovskite layers. The perovskite coated on PAA@SnO_2 was also discovered to be bigger than that coated on the SnO_2 layers. Additionally, as shown in Figure S8, the effects of various PAA concentrations in a SnO_2 colloidal solution on the surface morphology of perovskite layers were also obtained. It can be determined that the crystal grains of the perovskite on PAA@SnO_2 (0.5 and 1.0 mg/mL) are more uniform with less white PbI_2 phase in comparison with those of the perovskite on pristine SnO_2 and PAA@SnO_2 (2.0 and 3.0 mg/mL). The result indicates that PAA@SnO_2 can facilitate a uniform distribution of nucleation sites. Given that the incorporation of PAA leads to reduced roughness in the ETL thin film, the presence of a pre-existing functional group (carboxylic acid) on the PAA surface readily bonds with SnO_2 to form hydrogen bonding, leading to nanoparticle disaggregation as well as the enhanced wetting properties of ETL for perovskite precursor solution.

By adjusting the PAA concentration and layer thickness, the performance of the device is maximized. To successfully enable electron transport for ETL, the concentration of insulating PAA in SnO_2 should be maintained to a minimum. According to Table S1, the PCE of devices increases as PAA concentration increases, and the fill factor achieves its maximum when PAA content reaches 1.0 mg mL^{-1}. Conversely, there was a decrease in device PCE as the concentration of PAA increased (e.g., 2.0 and 3.0 mg mL^{-1}), which is thought to decrease the presence of SnO_2 nanoparticles in solution. Furthermore, the high affinity between PAA and SnO_2 contributes significantly to the formation of nanoparticle aggregations. Additionally, due to the weak conductivity of SnO_2 produced at low temper-

atures, the layer thickness should be as thin as possible while still preventing significant current leakage. For both pure SnO_2 and $PAA@SnO_2$, a well-defined boundary between each layer indicates thick coatings on the substrate, as shown in Figure S9a,b. Notably, the $PAA@SnO_2$ layer is significantly thinner (approximately 35 nm) when compared to pure SnO_2 (approximately 69 nm). The polymer matrix reduces the thickness of the ETL by approximately 50%, a substantial reduction when compared to the majority of ETLs reported in literature [68,69], which can enhance ETL light transmission and decrease series resistance. Furthermore, the thicknesses of the perovskite, spiro-OMeTAD, and metal electrode (Au) layers are approximately 560 nm, 195 nm, and 30 nm, respectively. Additionally, cross-section SEM images show that the surface roughness of pristine SnO_2 is higher than that of $PAA@SnO2$ (Figure S9c,d). This highlights the advantages of using polymer doping materials, especially those with functional groups on their surfaces, such as PAA in this study.
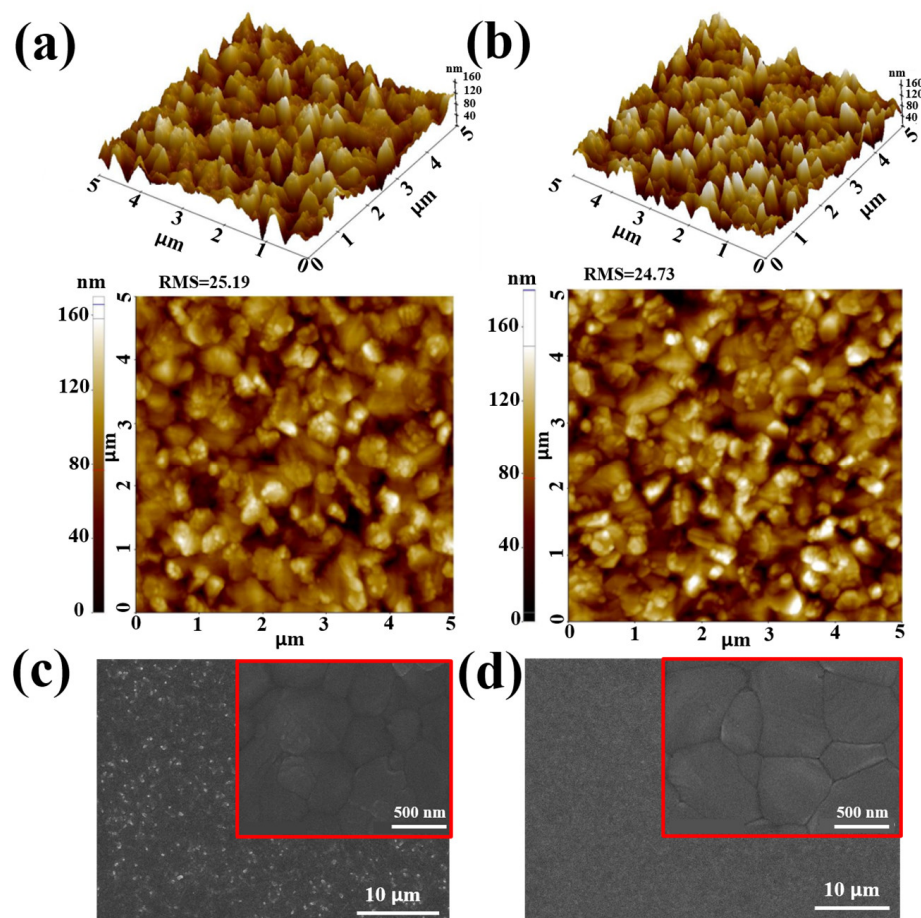

Figure 8. AFM images of perovskite coated on (**a**) SnO_2 and (**b**) $PAA@SnO_2$ layer. Top-view of SEM images of perovskite coated on (**c**) SnO_2 and (**d**) $PAA@SnO_2$ films.

UV–Vis spectroscopy was used to assess the light-harvesting capabilities of perovskites with varied SnO_2 and $PAA@SnO_2$ ETLs (Figure 9a). Evidently, the $PAA@SnO_2$ layer has a minor impact on the perovskite layer's capacity for absorption. Nevertheless, its bandgap has not changed. From the Tauc plot in Figure S10, the value of Eg is estimated to be 2.05 eV, and there is not much difference in Eg between $PAA@SnO_2$ and pristine SnO_2. Therefore, doping PAA does not significantly affect the pristine SnO_2 structure for the formation of the perovskite layer. Figure 9b,c show the steady-state photoluminescence (PL) of the absorber produced on different films. The PL peaks of the perovskite on SnO_2 and $PAA@SnO_2$ can be shown to have been significantly quenched, demonstrating a perfect band-edge alignment of SnO_2 with perovskite (Figure 9b). The PL intensity of the perovskite film on the surface

of the PAA@SnO$_2$ film is greater than that observed on the SnO$_2$ film under the identical test conditions. The perovskite layer on PAA@SnO$_2$ may have undergone less nonradiative recombination due to the stronger PL intensity [70–73]. Additionally, the perovskite film's PL peak on the PAA@SnO$_2$ ETL shifts by around 1.1 nm to a lower wavelength, which signals fewer defects (Figure 9c) [74]. Using PAA-incorporated SnO$_2$, the performance of PSC will be increased for two reasons, according to an examination of the characteristics of PAA@SnO$_2$ when compared to virgin SnO$_2$ (Figure 9d). First, pinholes can be minimized for film thicknesses under 40 nm by inhibiting nanoparticle aggregation, resulting in a more compact and homogeneous surface. Second, the PAA polymer can enhance the substrate's wetting properties.
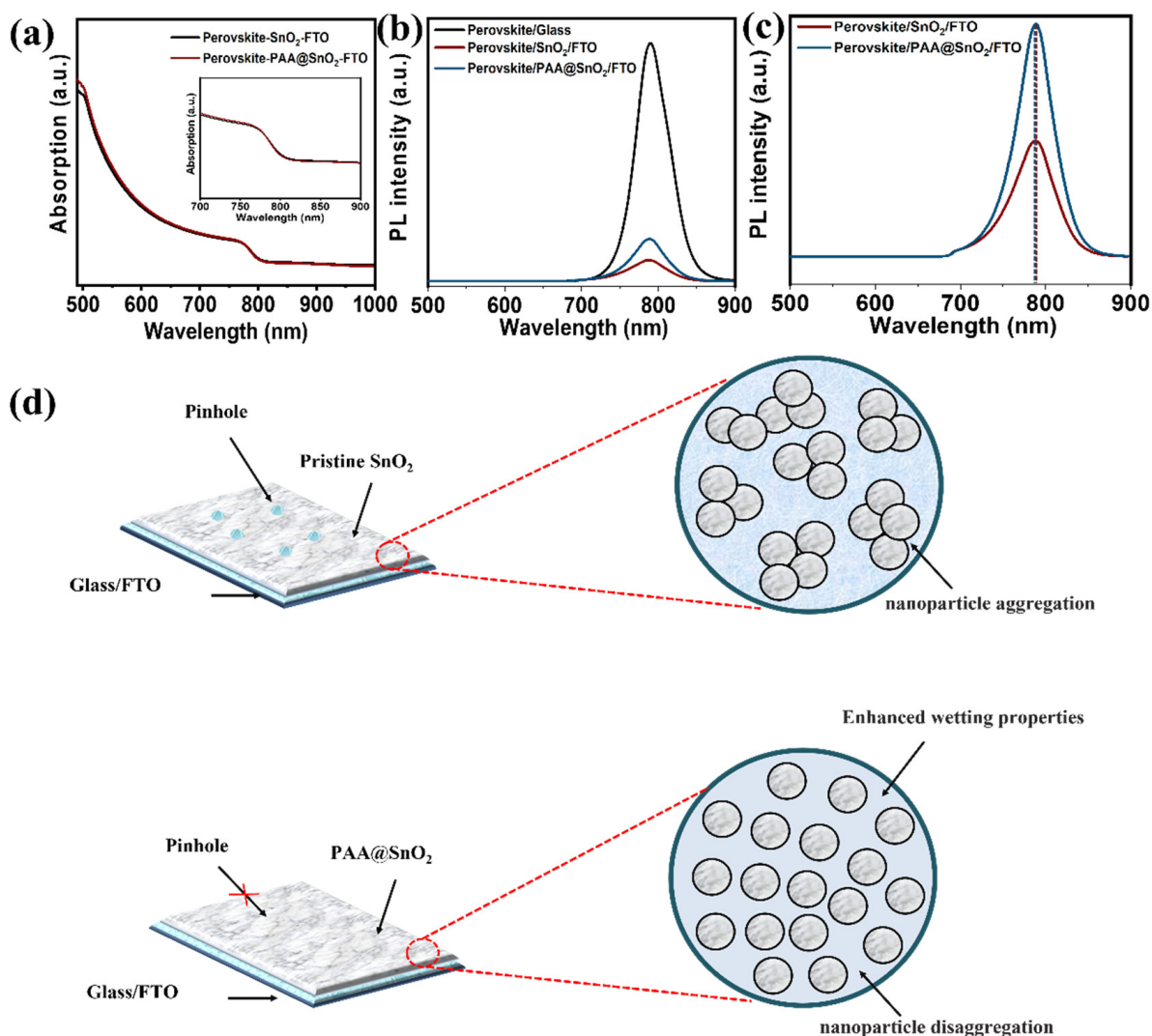

Figure 9. (**a**) UV−Vis absorption data of absorber films with SnO$_2$ and PAA@SnO$_2$ layers (the inset is amplifying absorption spectra in the wavelength range of 700−900 nm). (**b,c**) Steady-state PL spectra. (**d**) The diagram of film morphology for SnO$_2$ and PAA@SnO$_2$.

Based on the aforementioned advantages, the photovoltaic properties of undoped and doped-based SnO$_2$ PSCs were evaluated. The J−V curves for SnO$_2$ and PAA@SnO$_2$-based devices in the reverse and forward scan directions are shown in Figures 10a,b and S11. Table 2 illustrates the PAA@SnO$_2$-based devices with high efficiency and J−V characteristics of the champion devices using ETLs. The devices based on the SnO$_2$ ETL substrate exhibit a maximum PCE of 15.7%, with the specific values of Voc = 1.06 V, Jsc = 22.39 mA cm^{-2}, and FF = 0.68. Surprisingly, by switching the control ETL to a PAA@SnO$_2$ ETL, the

detailed parameters of Voc and FF were considerably enhanced to 1.08 V and 0.73%, respectively. Furthermore, the optimal PCE can be increased to 17.2%. This study shows that interfacial carrier recombination was significantly reduced by the PAA@SnO$_2$ layer's ability to passivate charge recombination at the ETL/perovskite interfaces. For each undoped and PAA-doped ETL, we created 20 different devices to test the repeatability of the material and technique, as shown in Table S2. The distribution of device parameters is shown in Figure 10c,d together with the statistical parameters that are presented in Figure S12. The J–V values for the doped SnO$_2$-based devices clearly show a narrow distribution with a low standard deviation, indicating exceptional repeatability.
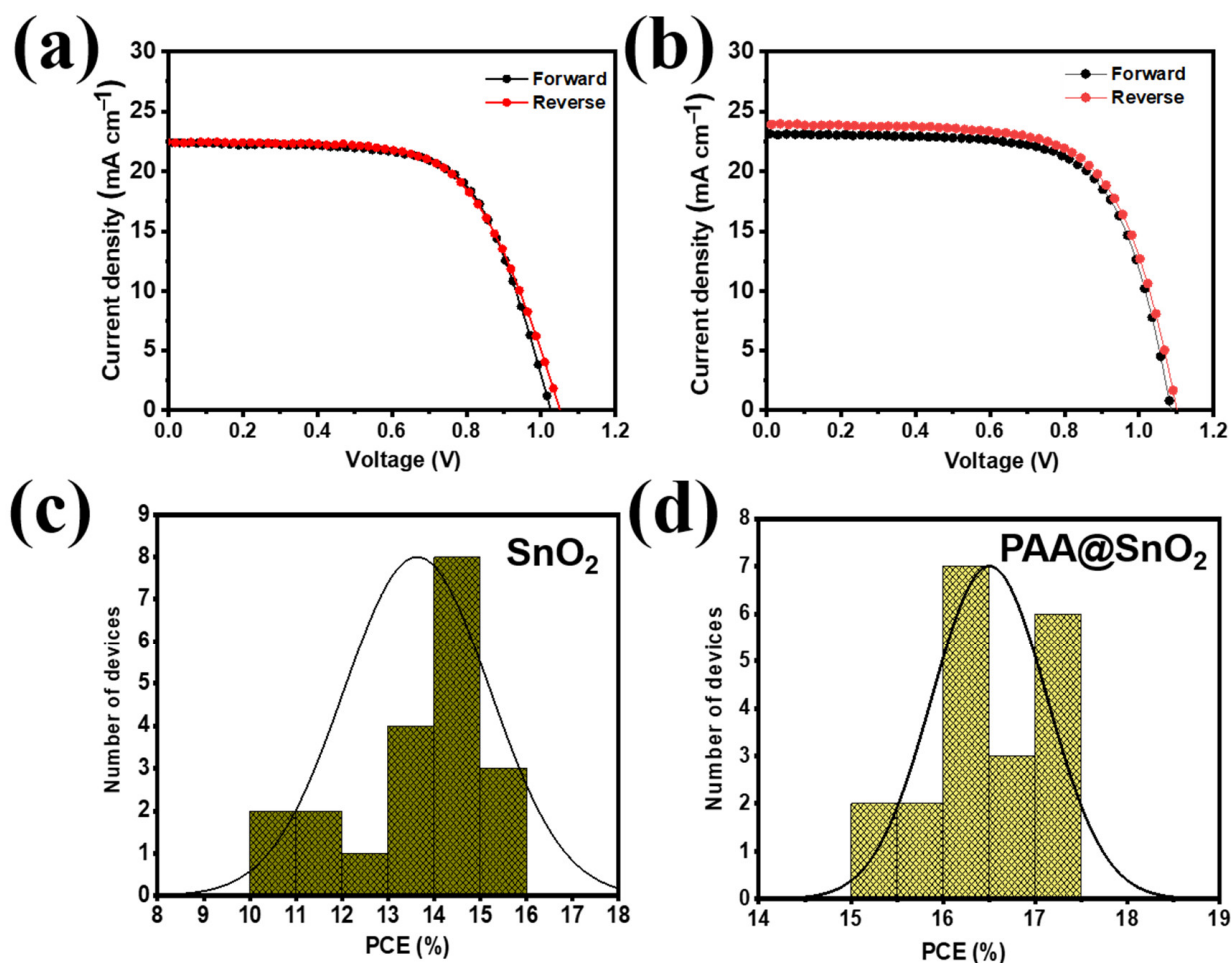

Figure 10. Current density−voltage (J−V) curves of devices based on (**a**) pristine SnO$_2$ and (**b**) PAA@SnO$_2$ with PAA concentration of 1.0 mg/mL under reverse-forward scanning directions. The PCE distribution of the PSCs of (**c**) SnO$_2$ and (**d**) PAA@SnO$_2$.

Table 2. Photovoltaic parameters of champion PSCs based on SnO$_2$ and PAA@SnO$_2$ ETLs.

Devices	Scan Direction	PCE (%)	J_{sc} (mA cm^{-2})	V_{oc} (V)	FF
SnO$_2$-PSC	Reverse	15.7	22.39	1.06	0.68
	Forward	15.2	21.85	1.03	0.66
PAA@SnO$_2$-PSC	Reverse	17.2	24.92	1.08	0.73
	Forward	16.8	23.12	1.07	0.69

The long-term stability of PSCs with SnO_2 and $PAA@SnO_2$ was evaluated in a nitrogen environment without encapsulation. Figure 11 illustrates the shelf stability of PSCs with different ETLs over time. After 30 days of storage, the device using the $PAA@SnO_2$ ETL retained 89% of its original power conversion efficiency (PCE), whereas the device with the SnO_2 ETL experienced a 21% reduction in its initial PCE. This indicates that devices with the $PAA@SnO_2$ ETL are more stable, likely due to improved contact between the $PAA@SnO_2$ ETL and perovskite layer. The degradation of the charge carrier transport layer and perovskite layer is a well-known factor contributing to the instability of PSCs. The enhanced stability in the $PAA@SnO_2$-based devices when compared to those with SnO_2 can be attributed to the improved interaction between the ETL and the perovskite layer.
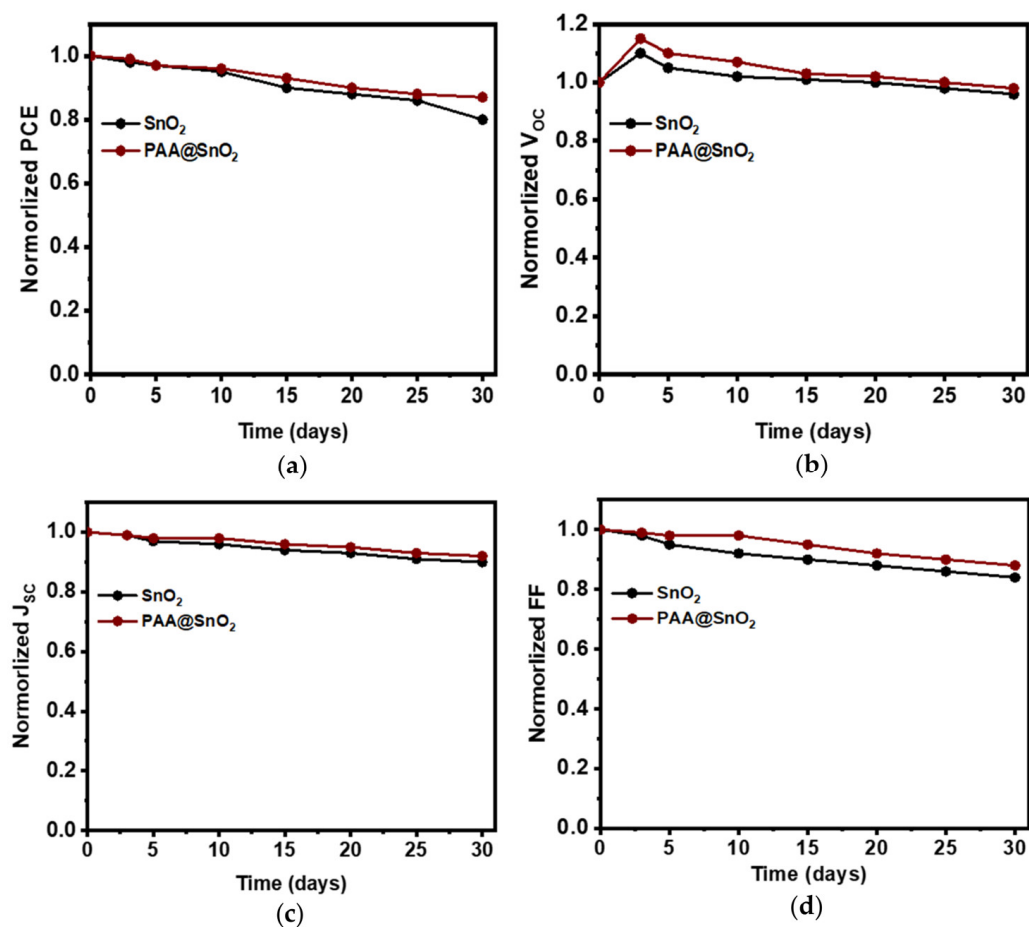

Figure 11. Shelf-stability of perovskite solar cells in a glove box without any encapsulation. Normalized (**a**) PCE, (**b**) V_{OC}, (**c**) J_{SC}, and (**d**) FF.

Table 3 summarizes the performance of PSCs with different doping materials in SnO_2 ETL. When compared to the performance of other recent PSCs, our $PAA@SnO_2$ exhibits performance increases from 15.7% to 17.2% (increase of approximately 10% in performance). It can be observed that doping with organic materials, specifically polymers, is slightly more effective than doping with inorganic materials due to the large particle size of the material, which easily forms large clusters on the ETL surface, contributing to reducing the surface contact between ETL and perovskite.

Table 3. Comparison of the performance of PAA@SnO$_2$ ETL in PSC with those of varying doping materials.

ETL	PCE (%)	V$_{OC}$ (V)	J$_{SC}$ (mA cm^{-2})	FF	Ref.
Pristine SnO$_2$	19.48	1.158	21.7	0.78	[75]
Ta-doped SnO$_2$	20.80	1.161	22.8	0.79	
Pristine SnO$_2$	15.31	1.078	23.2	0.61	[76]
Zn-doped SnO$_2$	17.78	1.098	23.4	0.69	
Pristine SnO$_2$	12.5	0.997	22.1	0.57	[77]
Ga-doped SnO$_2$	17.0	1.070	22.8	0.70	
Pristine SnO$_2$	12.32	0.88	22.8	0.61	[78]
Nb-doped SnO$_2$	13.53	0.92	24.1	0.61	
Pristine SnO$_2$	14.24	1.060	20.7	0.65	[79]
La-doped SnO$_2$	17.08	1.090	21.8	0.72	
Pristine SnO$_2$	11.69	1.030	18.6	0.61	[80]
Y-doped SnO$_2$	15.60	1.070	21.8	0.67	
Pristine SnO$_2$	15.07	1.020	21.0	0.59	[81]
Cl-doped SnO$_2$	18.10	1.110	23.0	0.69	
Pristine SnO$_2$	9.02	1.000	16.8	0.53	[65]
Al-doped SnO$_2$	12.10	1.030	19.4	0.58	
Pristine SnO$_2$	13.40	1.180	14.6	0.78	[71]
KF-doped SnO$_2$	15.39	1.310	14.8	0.79	
Pristine SnO$_2$	18.05	1.100	21.0	0.79	[50]
PVP-doped SnO$_2$	19.42	1.130	21.1	0.81	
Pristine SnO$_2$	18.60	1.070	22.6	0.77	[49]
PEG-doped SnO$_2$	20.80	1.110	22.7	0.82	
Pristine SnO$_2$	15.70	1.06	22.4	0.68	This
PAA-doped SnO$_2$	17.20	1.08	24.9	0.73	work

4. Conclusions

In summary, a straightforward and cost-effective technique has been suggested for the incorporation of PAA into the SnO$_2$ matrix to create a high-quality electron-selective layer. The PAA@SnO$_2$ layer, characterized by its dense and uniform structure with an ultra-thin thickness below 40 nm, is attributed to the enhanced dispersibility of the SnO$_2$ substrate. Due to the enhanced wetting properties of the polymer-modified film, a pinhole-free and high-quality perovskite film is easily formed on the PAA@SnO$_2$ matrix. Effective PSCs based on the PAA@SnO$_2$ matrix have been demonstrated, achieving a power conversion efficiency of 17.2% with high repeatability and shelf stability. This study presents a novel perspective on the inclusion of polymers as electron/hole selective layers in colloidal quantum dot inks. It is anticipated that future research and development involving other inorganic nanoparticle inks combined with suitable polymers will enhance device performance. This study highlights a new approach in the simple combination of polymers with metal oxides, acting as an effective electron/hole selective layer. The development of different polymers with suitable metal oxides is expected to further improve the current performance of devices. This process is promising in its simplicity and effectiveness, promoting its potential widespread application on an industrial scale.

Author Contributions: Investigation, V.P.H.H.; data curation, V.P.H.H.; writing—original draft preparation, V.P.H.H.; conceptualization, C.-W.B.; methodology, C.-W.B.; writing—review and editing, C.-W.B.; supervision, C.-W.B.; funding acquisition, C.-W.B. All authors have read and agreed to the published version of the manuscript.

Conflicts of Interest: The authors declare that they have no known competing financial interests or personal relationships that could have appeared to influence the work reported in this paper.

References

1. Miyata, A.; Mitioglu, A.; Plochocka, P.; Portugall, O.; Wang, J.T.-W.; Stranks, S.D.; Snaith, H.J.; Nicholas, R.J. Direct measurement of the exciton binding energy and effective masses for charge carriers in organic–inorganic tri-halide perovskites. *Nat. Phys.* **2015**, *11*, 582–587. [CrossRef]
2. Snaith, H.J. Perovskites: The Emergence of a New Era for Low-Cost, High-Efficiency Solar Cells. *J. Phys. Chem. Lett.* **2013**, *4*, 3623–3630. [CrossRef]
3. Jung, H.S.; Park, N. Perovskite Solar Cells: From Materials to Devices. *Small* **2015**, *11*, 10–25. [CrossRef]
4. Yang, L.; Barrows, A.T.; Lidzey, D.G.; Wang, T. Recent progress and challenges of organometal halide perovskite solar cells. *Rep. Prog. Phys.* **2016**, *79*, 026501. [CrossRef]
5. Park, J.; Kim, J.; Yun, H.-S.; Paik, M.J.; Noh, E.; Mun, H.J.; Kim, M.G.; Shin, T.J.; Seok, S.I. Controlled growth of perovskite layers with volatile alkylammonium chlorides. *Nature* **2023**, *616*, 724–730. [CrossRef]
6. Ma, F.; Zhao, Y.; Qu, Z.; You, J. Developments of Highly Efficient Perovskite Solar Cells. *Accounts Mater. Res.* **2023**, *4*, 716–725. [CrossRef]
7. Tiwari, S.K.; Shankar, G.; Kumar, P.; Laref, A.; Pradhan, B. Efficiency Approaching 26% in Triple Cation Mixed Halide Perovskite Solar Cells by Numerical Simulation. *IEEE J. Photovolt.* **2023**, *13*, 242–249. [CrossRef]
8. Yoshikawa, K.; Kawasaki, H.; Yoshida, W.; Irie, T.; Konishi, K.; Nakano, K.; Uto, T.; Adachi, D.; Kanematsu, M.; Uzu, H.; et al. Silicon heterojunction solar cell with interdigitated back contacts for a photoconversion efficiency over 26%. *Nat. Energy* **2017**, *2*, 17032. [CrossRef]
9. Bush, K.A.; Bailie, C.D.; Chen, Y.; Bowring, A.R.; Wang, W.; Ma, W.; Leijtens, T.; Moghadam, F.; McGehee, M.D. Thermal and Environmental Stability of Semi-Transparent Perovskite Solar Cells for Tandems Enabled by a Solution-Processed Nanoparticle Buffer Layer and Sputtered ITO Electrode. *Adv. Mater.* **2016**, *28*, 3937–3943. [CrossRef]
10. Grätzel, M. The Rise of Highly Efficient and Stable Perovskite Solar Cells. *Accounts Chem. Res.* **2017**, *50*, 487–491. [CrossRef]
11. Ono, L.K.; Park, N.-G.; Zhu, K.; Huang, W.; Qi, Y. Perovskite Solar Cells—Towards Commercialization. *ACS Energy Lett.* **2017**, *2*, 1749–1751. [CrossRef]
12. Wang, Y.; Li, S.; Zhang, P.; Liu, D.; Gu, X.; Sarvari, H.; Ye, Z.; Wu, J.; Wang, Z.; Chen, Z.D. Solvent annealing of PbI_2 for the high-quality crystallization of perovskite films for solar cells with efficiencies exceeding 18%. *Nanoscale* **2016**, *8*, 19654–19661. [CrossRef]
13. Domanski, K.; Alharbi, E.A.; Hagfeldt, A.; Grätzel, M.; Tress, W. Systematic investigation of the impact of operation conditions on the degradation behaviour of perovskite solar cells. *Nat. Energy* **2018**, *3*, 61–67. [CrossRef]
14. Snaith, H.J.; Abate, A.; Ball, J.M.; Eperon, G.E.; Leijtens, T.; Noel, N.K.; Stranks, S.D.; Wang, J.T.-W.; Wojciechowski, K.; Zhang, W. Anomalous Hysteresis in Perovskite Solar Cells. *J. Phys. Chem. Lett.* **2014**, *5*, 1511–1515. [CrossRef]
15. Wei, J.; Li, H.; Zhao, Y.; Zhou, W.; Fu, R.; Leprince-Wang, Y.; Yu, D.; Zhao, Q. Suppressed hysteresis and improved stability in perovskite solar cells with conductive organic network. *Nano Energy* **2016**, *26*, 139–147. [CrossRef]
16. Zhao, Y.; Zhou, W.; Ma, W.; Meng, S.; Li, H.; Wei, J.; Fu, R.; Liu, K.; Yu, D.; Zhao, Q. Correlations between Immobilizing Ions and Suppressing Hysteresis in Perovskite Solar Cells. *ACS Energy Lett.* **2016**, *1*, 266–272. [CrossRef]
17. Wei, J.; Shi, C.; Zhao, Y.; Zhou, W.; Li, H.; Fu, R.; Yu, D.; Zhao, Q. Potentials and challenges towards application of perovskite solar cells. *Sci. China Mater.* **2016**, *59*, 769–778. [CrossRef]
18. Shao, Y.; Xiao, Z.; Bi, C.; Yuan, Y.; Huang, J. Origin and elimination of photocurrent hysteresis by fullerene passivation in CH3NH3PbI3 planar heterojunction solar cells. *Nat. Commun.* **2014**, *5*, 5784. [CrossRef]
19. Nie, W.; Tsai, H.; Blancon, J.; Liu, F.; Stoumpos, C.C.; Traore, B.; Kepenekian, M.; Durand, O.; Katan, C.; Tretiak, S.; et al. Critical Role of Interface and Crystallinity on the Performance and Photostability of Perovskite Solar Cell on Nickel Oxide. *Adv. Mater.* **2018**, *30*, 1703879. [CrossRef]
20. Wang, Y.; Wan, J.; Ding, J.; Hu, J.; Wang, D. A Rutile TiO_2 Electron Transport Layer for the Enhancement of Charge Collection for Efficient Perovskite Solar Cells. *Angew. Chem. Int. Ed.* **2019**, *58*, 9414–9418. [CrossRef] [PubMed]

21. Wang, J.; Pan, H.; Xu, X.; Jin, H.; Ma, W.; Xiong, S.; Bao, Q.; Tang, Z.; Ma, Z. Li-Doped ZnO Electron Transport Layer for Improved Performance and Photostability of Organic Solar Cells. *ACS Appl. Mater. Interfaces* **2022**, *14*, 12450–12460. [CrossRef] [PubMed]

22. Jiang, J.; Lang, X.; Zeng, Q.; Faheem, M.B.; Rong, S.; Zhao, H.; Li, Y. Polyacetylene derivatives in perovskite solar cells: From defect passivation to moisture endurance. *J. Mater. Chem. A* **2021**, *9*, 13220–13230. [CrossRef]

23. Liu, X.; Chueh, C.-C.; Zhu, Z.; Jo, S.B.; Sun, Y.; Jen, A.K.-Y. Highly crystalline Zn$_2$SnO$_4$ nanoparticles as efficient electron-transporting layers toward stable inverted and flexible conventional perovskite solar cells. *J. Mater. Chem. A* **2016**, *4*, 15294–15301. [CrossRef]

24. Hu, W.; Liu, T.; Yin, X.; Liu, H.; Zhao, X.; Luo, S.; Guo, Y.; Yao, Z.; Wang, J.; Wang, N.; et al. Hematite electron-transporting layers for environmentally stable planar perovskite solar cells with enhanced energy conversion and lower hysteresis. *J. Mater. Chem. A* **2017**, *5*, 1434–1441. [CrossRef]

25. Zhang, X.; Li, J.; Bi, Z.; He, K.; Xu, X.; Xiao, X.; Zhu, Y.; Zhan, Y.; Zhong, L.; Xu, G.; et al. Stable and efficient air-processed perovskite solar cells employing low-temperature processed compact In$_2$O$_3$ thin films as electron transport materials. *J. Alloys Compd.* **2020**, *836*, 155460. [CrossRef]

26. Mo, Y.; Wang, C.; Zheng, X.; Zhou, P.; Li, J.; Yu, X.; Yang, K.; Deng, X.; Park, H.; Huang, F.; et al. Nitrogen-doped tin oxide electron transport layer for stable perovskite solar cells with efficiency over 23%. *Interdiscip. Mater.* **2022**, *1*, 309–315. [CrossRef]

27. Tan, H.; Jain, A.; Voznyy, O.; Lan, X.; de Arquer, F.P.G.; Fan, J.Z.; Quintero-Bermudez, R.; Yuan, M.; Zhang, B.; Zhao, Y.; et al. Efficient and stable solution-processed planar perovskite solar cells via contact passivation. *Science* **2017**, *355*, 722–726. [CrossRef] [PubMed]

28. Tress, W.; Marinova, N.; Moehl, T.; Zakeeruddin, S.M.; Nazeeruddin, M.K.; Grätzel, M. Understanding the rate-dependent J–V hysteresis, slow time component, and aging in CH3NH3PbI3 perovskite solar cells: The role of a compensated electric field. *Energy Environ. Sci.* **2015**, *8*, 995–1004. [CrossRef]

29. Zhang, M.; Yan, K.; Han, W.; Yang, S. One-pot Synthesis of Mesoporous TiO$_2$ from Self-Assembled Sol Particles and Its Application as Mesoscopic Photoanodes of Dye-Sensitized Solar Cells. *Chempluschem* **2013**, *78*, 647–655. [CrossRef]

30. Yang, D.; Zhou, X.; Yang, R.; Yang, Z.; Yu, W.; Wang, X.; Li, C.; Liu, S.; Chang, R.P.H. Surface optimization to eliminate hysteresis for record efficiency planar perovskite solar cells. *Energy Environ. Sci.* **2016**, *9*, 3071–3078. [CrossRef]

31. Son, D.-Y.; Lee, J.-W.; Choi, Y.J.; Jang, I.-H.; Lee, S.; Yoo, P.J.; Shin, H.; Ahn, N.; Choi, M.; Kim, D.; et al. Self-formed grain boundary healing layer for highly efficient CH3NH3PbI3 perovskite solar cells. *Nat. Energy* **2016**, *1*, 16081. [CrossRef]

32. Shin, S.S.; Yeom, E.J.; Yang, W.S.; Hur, S.; Kim, M.G.; Im, J.; Seo, J.; Noh, J.H.; Seok, S.I. Colloidally prepared La-doped BaSnO3 electrodes for efficient, photostable perovskite solar cells. *Science* **2017**, *356*, 167–171. [CrossRef] [PubMed]

33. Luo, J.; Chen, J.; Wu, B.; Goh, T.W.; Qiao, W.; Ku, Z.; Bin Yang, H.; Zhang, L.; Sum, T.C.; Liu, B. Surface Rutilization of Anatase TiO$_2$ for Efficient Electron Extraction and Stable Pmax Output of Perovskite Solar Cells. *Chem* **2018**, *4*, 911–923. [CrossRef]

34. Yang, D.; Yang, R.; Wang, K.; Wu, C.; Zhu, X.; Feng, J.; Ren, X.; Fang, G.; Priya, S.; Liu, S. High efficiency planar-type perovskite solar cells with negligible hysteresis using EDTA-complexed SnO$_2$. *Nat. Commun.* **2018**, *9*, 3239. [CrossRef] [PubMed]

35. Jiang, Q.; Chu, Z.; Wang, P.; Yang, X.; Liu, H.; Wang, Y.; Yin, Z.; Wu, J.; Zhang, X.; You, J. Planar-Structure Perovskite Solar Cells with Efficiency beyond 21%. *Adv. Mater.* **2017**, *29*, 1703852. [CrossRef] [PubMed]

36. Jiang, Q.; Zhang, L.; Wang, H.; Yang, X.; Meng, J.; Liu, H.; Yin, Z.; Wu, J.; Zhang, X.; You, J. Enhanced electron extraction using SnO$_2$ for high-efficiency planar-structure HC(NH2)2PbI3-based perovskite solar cells. *Nat. Energy* **2016**, *2*, 16177. [CrossRef]

37. Wu, W.; Chen, D.; Cheng, Y.; Caruso, R.A. Thin Films of Tin Oxide Nanosheets Used as the Electron Transporting Layer for Improved Performance and Ambient Stability of Perovskite Photovoltaics. *Sol. RRL* **2017**, *1*, 1700117. [CrossRef]

38. Ke, W.; Fang, G.; Liu, Q.; Xiong, L.; Qin, P.; Tao, H.; Wang, J.; Lei, H.; Li, B.; Wan, J.; et al. Low-Temperature Solution-Processed Tin Oxide as an Alternative Electron Transporting Layer for Efficient Perovskite Solar Cells. *J. Am. Chem. Soc.* **2015**, *137*, 6730–6733. [CrossRef]

39. Dong, Q.; Shi, Y.; Wang, K.; Li, Y.; Wang, S.; Zhang, H.; Xing, Y.; Du, Y.; Bai, X.; Ma, T. Insight into Perovskite Solar Cells Based on SnO$_2$ Compact Electron-Selective Layer. *J. Phys. Chem. C* **2015**, *119*, 10212–10217. [CrossRef]

40. Baena, J.P.C.; Steier, L.; Tress, W.; Saliba, M.; Neutzner, S.; Matsui, T.; Giordano, F.; Jacobsson, T.J.; Kandada, A.R.S.; Zakeeruddin, S.M.; et al. Highly efficient planar perovskite solar cells through band alignment engineering. *Energy Environ. Sci.* **2015**, *8*, 2928–2934. [CrossRef]

41. Bai, Y.; Fang, Y.; Deng, Y.; Wang, Q.; Zhao, J.; Zheng, X.; Zhang, Y.; Huang, J. Low Temperature Solution-Processed Sb:SnO$_2$ Nanocrystals for Efficient Planar Perovskite Solar Cells. *ChemSusChem* **2016**, *9*, 2686–2691. [CrossRef] [PubMed]

42. Park, M.; Kim, J.-Y.; Son, H.J.; Lee, C.-H.; Jang, S.S.; Ko, M.J. Low-temperature solution-processed Li-doped SnO$_2$ as an effective electron transporting layer for high-performance flexible and wearable perovskite solar cells. *Nano Energy* **2016**, *26*, 208–215. [CrossRef]

43. Anaraki, E.H.; Kermanpur, A.; Steier, L.; Domanski, K.; Matsui, T.; Tress, W.; Saliba, M.; Abate, A.; Grätzel, M.; Hagfeldt, A.; et al. Highly efficient and stable planar perovskite solar cells by solution-processed tin oxide. *Energy Environ. Sci.* **2016**, *9*, 3128–3134. [CrossRef]

44. Dagar, J.; Castro-Hermosa, S.; Lucarelli, G.; Cacialli, F.; Brown, T.M. Highly efficient perovskite solar cells for light harvesting under indoor illumination via solution processed SnO$_2$/MgO composite electron transport layers. *Nano Energy* **2018**, *49*, 290–299. [CrossRef]

45. Bahadur, J.; Ghahremani, A.H.; Martin, B.; Druffel, T.; Sunkara, M.K.; Pal, K. Solution processed Mo doped SnO_2 as an effective ETL in the fabrication of low temperature planer perovskite solar cell under ambient conditions. *Org. Electron.* **2019**, *67*, 159–167. [CrossRef]

46. Ahmed, A.; Riaz, K.; Mehmood, H.; Tauqeer, T.; Ahmad, Z. Performance optimization of CH3NH3Pb(I1-xBrx)3 based perovskite solar cells by comparing different ETL materials through conduction band offset engineering. *Opt. Mater.* **2020**, *105*, 109897. [CrossRef]

47. Aygüler, M.F.; Hufnagel, A.G.; Rieder, P.; Wussler, M.; Jaegermann, W.; Bein, T.; Dyakonov, V.; Petrus, M.L.; Baumann, A.; Docampo, P. Influence of Fermi Level Alignment with Tin Oxide on the Hysteresis of Perovskite Solar Cells. *ACS Appl. Mater. Interfaces* **2018**, *10*, 11414–11419. [CrossRef]

48. Anefnaf, I.; Aazou, S.; Schmerber, G.; Refki, S.; Zimmermann, N.; Heiser, T.; Ferblantier, G.; Slaoui, A.; Dinia, A.; Abd-Lefdil, M.; et al. Polyethylenimine-Ethoxylated Interfacial Layer for Efficient Electron Collection in SnO_2-Based Inverted Organic Solar Cells. *Crystals* **2020**, *10*, 731. [CrossRef]

49. Wei, J.; Guo, F.; Wang, X.; Xu, K.; Lei, M.; Liang, Y.; Zhao, Y.; Xu, D. SnO_2-in-Polymer Matrix for High-Efficiency Perovskite Solar Cells with Improved Reproducibility and Stability. *Adv. Mater.* **2018**, *30*, 1805153. [CrossRef]

50. Wang, D.; Chen, S.-C.; Zheng, Q. Poly(vinylpyrrolidone)-doped SnO_2 as an electron transport layer for perovskite solar cells with improved performance. *J. Mater. Chem. C* **2019**, *7*, 12204–12210. [CrossRef]

51. Cevik, E.; Bozkurt, A. Redox active polymer metal chelates for use in flexible symmetrical supercapacitors: Cobalt-containing poly(acrylic acid) polymer electrolytes. *J. Energy Chem.* **2021**, *55*, 145–153. [CrossRef]

52. Braam, K.; Subramanian, V. A Stencil Printed, High Energy Density Silver Oxide Battery Using a Novel Photopolymerizable Poly(acrylic acid) Separator. *Adv. Mater.* **2015**, *27*, 689–694. [CrossRef] [PubMed]

53. Huy, V.P.H.; So, S.; Kim, I.T.; Hur, J. Self-healing gallium phosphide embedded in a hybrid matrix for high-performance Li-ion batteries. *Energy Storage Mater.* **2021**, *34*, 669–681. [CrossRef]

54. Lakshminarasimhan, N.; Kim, W.; Choi, W. Effect of the Agglomerated State on the Photocatalytic Hydrogen Production with in Situ Agglomeration of Colloidal TiO_2 Nanoparticles. *J. Phys. Chem. C* **2008**, *112*, 20451–20457. [CrossRef]

55. Li, F.; Deng, X.; Qi, F.; Li, Z.; Liu, D.; Shen, D.; Qin, M.; Wu, S.; Lin, F.; Jang, S.-H.; et al. Regulating Surface Termination for Efficient Inverted Perovskite Solar Cells with Greater Than 23% Efficiency. *J. Am. Chem. Soc.* **2020**, *142*, 20134–20142. [CrossRef] [PubMed]

56. Yang, J.K.; Liang, B.; Zhao, M.J.; Gao, Y.; Zhang, F.C.; Zhao, H.L. Reference of Temperature and Time during tempering process for non-stoichiometric FTO films. *Sci. Rep.* **2015**, *5*, 15001. [CrossRef] [PubMed]

57. Sayah, A.; Habelhames, F.; Bahloul, A.; Boudjadi, A. The effect of electrodeposition applied potential on the electrochemical performance of polyaniline films. *J. Mater. Sci. Mater. Electron.* **2021**, *32*, 10692–10701. [CrossRef]

58. Khan, M.; Parveen, A. Microwave Assisted Synthesis of Graphene/SnO_2 Nanocomposite and its Structural, Dielectric and Electrical Properties. *J. Nanotechnol. Res.* **2020**, *2*, 10–24. [CrossRef]

59. Phuoc, P.H.; Hung, C.M.; Van Toan, N.; Van Duy, N.; Hoa, N.D.; Van Hieu, N. One-step fabrication of SnO_2 porous nanofiber gas sensors for sub-ppm H2S detection. *Sens. Actuators A Phys.* **2020**, *303*, 111722. [CrossRef]

60. Sameea, N.; Hassaan, M.; Tiama, T.M. Development and In-Vivo Histological evaluation of the biocompatibility of glass ionomer Cement Prepared by sol–gel Method. *EC Dent. Sci.* **2017**, *12*, 18–38.

61. Wang, C.; Wu, H.; Chen, Z.; McDowell, M.T.; Cui, Y.; Bao, Z. Self-healing chemistry enables the stable operation of silicon microparticle anodes for high-energy lithium-ion batteries. *Nat. Chem.* **2013**, *5*, 1042–1048. [CrossRef] [PubMed]

62. Xu, C.; Liu, Z.; Sun, Q.; Lee, E.-C. Morphology control of SnO_2 layer by solvent engineering for efficient perovskite solar cells. *Sol. Energy* **2021**, *214*, 280–287. [CrossRef]

63. Zamani, M.R.; Keshtmand, R. Surface Modification of the SnO_2 Layer Using UV-Ozone in a Perovskite Solar Cell with a Planar Structure. *IUST* **2021**, *18*, 1–9.

64. Yu, H.; Yeom, H.; Lee, J.W.; Lee, K.; Hwang, D.; Yun, J.; Ryu, J.; Lee, J.; Bae, S.; Kim, S.K.; et al. Superfast Room-Temperature Activation of SnO_2 Thin Films via Atmospheric Plasma Oxidation and their Application in Planar Perovskite Photovoltaics. *Adv. Mater.* **2018**, *30*, 1704825. [CrossRef] [PubMed]

65. Chen, H.; Liu, D.; Wang, Y.; Wang, C.; Zhang, T.; Zhang, P.; Sarvari, H.; Chen, Z.; Li, S. Enhanced Performance of Planar Perovskite Solar Cells Using Low-Temperature Solution-Processed Al-Doped SnO_2 as Electron Transport Layers. *Nanoscale Res. Lett.* **2017**, *12*, 238. [CrossRef]

66. Kim, S.; Bark, C.W. Effect of Surface Treatment by Chemical-Mechanical Polishing for Transparent Electrode of Perovskite Solar Cells. *Energies* **2020**, *13*, 585. [CrossRef]

67. Cojocaru, L.; Uchida, S.; Jayaweera, P.V.; Kaneko, S.; Wang, H.; Nakazaki, J.; Kubo, T.; Segawa, H. Effect of TiO_2 surface treatment on the I-V hysteresis of planar structure perovskite solar cells prepared on rough and flat FTO substrates. *Energy Technol.* **2017**, *5*, 1762–1766. [CrossRef]

68. Liu, X.; Zhang, Y.; Shi, L.; Liu, Z.; Huang, J.; Yun, J.S.; Zeng, Y.; Pu, A.; Sun, K.; Hameiri, Z.; et al. Exploring Inorganic Binary Alkaline Halide to Passivate Defects in Low-Temperature-Processed Planar-Structure Hybrid Perovskite Solar Cells. *Adv. Energy Mater.* **2018**, *8*. [CrossRef]

69. Lin, C.C.; Murakami, T.N.; Chikamatsu, M.; Bessho, T.; Furue, M.; Segawa, H. A Sodium Chloride Modification of SnO_2 Electron Transport Layers to Enhance the Performance of Perovskite Solar Cells. *ACS Omega* **2021**, *6*, 17880–17889. [CrossRef]

70. Kim, S.; Zhang, F.; Tong, J.; Chen, X.; Enkhbayar, E.; Zhu, K.; Kim, J. Effects of potassium treatment on SnO_2 electron transport layers for improvements of perovskite solar cells. *Sol. Energy* **2022**, *233*, 353–362. [CrossRef]

71. Zhang, S.; Gu, H.; Chen, S.-C.; Zheng, Q. KF-Doped SnO_2 as an electron transport layer for efficient inorganic $CsPbI_2Br$ perovskite solar cells with enhanced open-circuit voltages. *J. Mater. Chem. C* **2021**, *9*, 4240–4247. [CrossRef]

72. Zhu, P.; Gu, S.; Luo, X.; Gao, Y.; Li, S.; Zhu, J.; Tan, H. Simultaneous Contact and Grain-Boundary Passivation in Planar Perovskite Solar Cells Using SnO_2-KCl Composite Electron Transport Layer. *Adv. Energy Mater.* **2020**, *10*, 1903083. [CrossRef]

73. Liu, Z.; Deng, K.; Hu, J.; Li, L. Coagulated SnO_2 Colloids for High-Performance Planar Perovskite Solar Cells with Negligible Hysteresis and Improved Stability. *Angew. Chem. Int. Ed.* **2019**, *58*, 11497–11504. [CrossRef] [PubMed]

74. Zhang, L.; Li, H.; Zhuang, J.; Luan, Y.; Wu, S.; Niu, G.; Chu, L.; Cao, X.; Li, X.; Wang, J. Antimony trifluoride-incorporated SnO_2 for high-efficiency planar perovskite solar cells. *J. Mater. Chem. C* **2021**, *9*, 15428–15434. [CrossRef]

75. Liu, Q.; Zhang, X.; Li, C.; Lu, H.; Weng, Z.; Pan, Y.; Chen, W.; Hang, X.-C.; Sun, Z.; Zhan, Y. Effect of tantalum doping on SnO_2 electron transport layer via low temperature process for perovskite solar cells. *Appl. Phys. Lett.* **2019**, *115*, 143903. [CrossRef]

76. Ye, H.; Liu, Z.; Liu, X.; Sun, B.; Tan, X.; Tu, Y.; Shi, T.; Tang, Z.; Liao, G. 17.78% efficient low-temperature carbon-based planar perovskite solar cells using Zn-doped SnO_2 electron transport layer. *Appl. Surf. Sci.* **2019**, *478*, 417–425. [CrossRef]

77. Roose, B.; Johansen, C.M.; Dupraz, K.; Jaouen, T.; Aebi, P.; Steiner, U.; Abate, A. A Ga-doped SnO_2 mesoporous contact for UV stable highly efficient perovskite solar cells. *J. Mater. Chem. A* **2018**, *6*, 1850–1857. [CrossRef]

78. Wang, S.; Shen, W.; Liu, J.; Ouyang, T.; Wu, Y.; Li, W.; Chen, M.; Qi, P.; Lu, Y.; Tang, Y. Improved photovoltage of printable perovskite solar cells via Nb5+ doped SnO_2 compact layer. *Nanotechnology* **2021**, *32*, 145403. [CrossRef]

79. Xu, Z.; Teo, S.H.; Gao, L.; Guo, Z.; Kamata, Y.; Hayase, S.; Ma, T. La-doped SnO_2 as ETL for efficient planar-structure hybrid perovskite solar cells. *Org. Electron.* **2019**, *73*, 62–68. [CrossRef]

80. Yang, G.; Lei, H.; Tao, H.; Zheng, X.; Ma, J.; Liu, Q.; Ke, W.; Chen, Z.; Xiong, L.; Qin, P.; et al. Reducing Hysteresis and Enhancing Performance of Perovskite Solar Cells Using Low-Temperature Processed Y-Doped SnO_2 Nanosheets as Electron Selective Layers. *Small* **2017**, *13*, 1601769. [CrossRef]

81. Gong, W.; Guo, H.; Zhang, H.; Yang, J.; Chen, H.; Wang, L.; Hao, F.; Niu, X. Chlorine-doped SnO_2 hydrophobic surfaces for large grain perovskite solar cells. *J. Mater. Chem. C* **2020**, *8*, 11638–11646. [CrossRef]